Numerical simulation of the effect of a DC electric field on a laminar ethylene diffusion flame

Ahmad Sayed-Kassem, Pascale Gillon, Mahmoud Idir, Abdallah Elorf, Virginie Gilard

Numerical simulation of the effect of a DC electric field on a laminar ethylene diffusion flame

Ahmad Sayed-Kassem[a,b]*, Pascale Gillon[a]*, Mahmoud Idir[a], Abdallah Elorf[a] and Virginie Gilard[a,b]

[a] CNRS-INSIS, ICARE laboratory, 1C avenue de la recherche scientifique 45071 Orléans cedex2, France
[b] Université d'Orléans, IUT, 45067 Orléans, France

* Corresponding authors are at ICARE laboratory of the CNRS (1C avenue de la recherche scientifique 45071 Orléans cedex2, France).

Email addresses: pascale.gillon@cnrs-orleans.fr (P. Gillon) and ahmad.sayed-kassem@cnrs-orleans.fr (A. Sayed-Kassem).

Highlights

- A numerical model was developed to simulate ethylene diffusion combustion and validated with experimental measurements.
- The developed model was extended to cover the effect of a DC electric field on ethylene non-premixed combustion.
- An applied electric field deforms the flame structure, promotes the combustion rate and modifies flame dynamic.
- Ionic wind is responsible for the observed modifications acting essentially near the burner exit.

Abstract

An applied DC electric field was experimentally demonstrated to modify the flame structure and gas dynamic in an ethylene diffusion flame. The aim of this paper is to investigate the influence of the electric field on the flow field and its impacts on the flame behavior. A numerical study has been performed to elucidate the experimental observations and to monitor the effect of electric body force on the flame. The numerical model was validated by comparing the computed results to experimental measurements from the literature. The resulting computed flame shape was compared to a visible image taken during the experiment. The simulated OH mole fraction, the burning rate and the computed velocity and temperature are presented. The developed model proved the ability to reproduce qualitatively the experimental flame behavior when submitted to the electric field. The electric field is shown to modify the flame shape (flame tip, flame shortness and flame deformation), to promote the burning process and to improve the ion production. Results show that the modifications are due to an air entrainment acting specifically near the burner zone enhancing the mixture and changing the fluid dynamic in this region. The ionic wind is demonstrated to increase the maximum burning rate and promoting ions' formation mostly near the burner. A more detailed model (detailed ions' chemistry and soot model with charged particles, detailed electric diffusion) is necessary to gain a better understanding of the influence of electric field on diffusion combustion and soot formation.

Keywords: Laminar diffusion flame, Electric field, Numerical simulation, Ethylene.

Nomenclature

a_{pi}	plank mean absorption coefficient for species *i*
D^e	electronic diffusion
D_i	molecular diffusion
e	elementary charge
E	electric field
f_s	soot volume fraction
F^e	electric force
g	gravitational acceleration
h	total sensible enthalpy
h_j	sensible enthalpy of species *j*
$\boldsymbol{J_j}$	diffusion flux of species j
k	thermal conductivity
k_b	Boltzmann constant
$k_{s,Plank}$	plank mean absorption coefficient for soot
m^0	mass of gas
m^e	electronic mass
n_c	net charge density
n_+	positive charge density
n_-	negative charge density
p	pressure
p_i	local partial pressure of species *i*
q_i	specie charge
$\dot{Q}$	combustion heat release
r	radial direction distance
T	temperature
T_b	atmospheric temperature
u	axial direction velocity
v	radial direction velocity
V	electric potential
ω_i	net rate of production of species *i*
Y_i	mass fraction of species *i*

Greek letters

ε_0	free space permittivity
κ^e	electronic mobility
κ_i	electric mobility of species *i*
ρ	gas density
μ	dynamic viscosity
σ	Stefan-Boltzmann constant

1. Introduction

With the worsening pollution crisis and fossil fuel reserves decline, combustion control technologies become mandatory in order to reduce emissions and enhance combustion efficiency. Among different ways of control such as plasma assisted combustion [1], aerodynamic controlled combustion [2], or even dilution [3], electric assisted combustion has proven to be a promising technique. As demonstrated in the literature, applying an electric field to combustion is able to control the stability

[4–6], to reduce soot emissions [7–9] and pollutants [10,11] and to change the flame structure [12–14]. Investigations of diffusion flame behavior when submitted to electric fields have been extensively studied. Although methane has been investigated as the most referenced fuel, ethylene has also been studied [9] in the objective to control soot particle formation. Various configurations of the diffusion flame have been tested: upward and downward [15] vertical injection, without and with co-injection of air and counter-flow flames [9] coupled with a variety of electric field direction. The ion driven motion due to the drift velocity of the produced ions in flames appears to be the most important factor that profoundly modifies the flow field. Despite the fact that the majority of the studies reported in literature are experimental, some numerical studies were developed to investigate the nature of the effects. Yamashita et al. [15] developed a numerical model in order to explain the voltage-current characteristic behavior of a capillary-fed methane diffusion flame. Considering only the positive ions, they reported that the ion driven motion is responsible for the increase of ion production rate which resembles the flame current observed experimentally. Belhi et al. [16,17] performed a direct numerical simulation (DNS) focusing on the mechanisms responsible for the improvement of the stability of a methane diffusion flame when submitted to DC electric fields. The authors showed that an electric field induces a decrease in the lift height and favors the flame anchorage to the burner. Rao and Honnery [18] developed a simplified model to predict the ion current characteristics during premixed methane oxidation in engine-like conditions. The model was able to predict the ion current under different conditions of pressure and equivalence ratio. A qualitatively agreement with experimental tendency was obtained but with a notable difference in ion current magnitude. Xu et al. [19] investigated numerically and experimentally the effect of a DC electric field on a micro scale bio-butanol diffusion flame. The authors assumed a constant electric field in the domain and described the flame behavior at different fuel flow rates. The electric field was proved to decrease the quenching flow rate and modify the flame highest temperature and the flame height. The model developed by Luo et al. [20,21] for a small ethanol diffusion flame includes the electric body forces generated by applied DC and AC electric fields. An enhancement in fuel/oxidizer mixing was observed coupled with an increase in chemical reaction rate. Belhi et al. [22] performed a 2D numerical simulation of counter-flow non-premixed flames under a DC electric field. A skeletal mechanism for methane

combustion was employed with a specific approximation to predict ions production rate and a different approach to compute transport properties. Several parameters of their model (CH prediction, chemi-ionization reaction rate, recombination reaction and transport coefficient) were tested in a 1D-numerical calculation of premixed flames [23]. The authors found that these parameters play an important role in predicting ions formation in a flame. More recently, the same model was integrated into an unsteady 3D simulation for a premixed methane flame under a transverse electric field in the saturation regime [24]. A quantitative agreement with experiments was obtained.

In the latest work [25], a laminar ethylene diffusion flame was experimentally investigated under the influence of a DC electric field. Here, a co-flow burner was used as a cathode. A grounded electrode was mounted at 140 mm above the burner exit in order to generate an upward electric field. Flame imaging was employed to monitor flame structure and Extinction/ Rayleigh Scattering optical diagnostic was applied to measure soot characteristics. Relevantly, when we applied an electric field, flame shortness with an enlargement was detected. Additionally, a reduction in soot volume fraction and soot number density was noted. These observations were mainly attributed to the ionic wind acting on the flow field and the soot formation process.

The main objective of this study is to investigate numerically the effects of the electric body forces on a flame which was studied previously experimentally [25]. In this work, a numerical model was developed for a laminar diffusion ethylene flame using the CFD software FLUENT. The electric field equation with the source terms for the governing equations were integrated to the model by implementing User Defined Functions (UDF) codes in the solver and resolving User Defined Scalar (UDS) equation for the potential. Here, the impact of electric field in gas dynamic during combustion is studied. The effect of electric field on the flame shape, combustion rate and flame temperature are also elucidated by comparing different results under different values of potential.

Model description

The experimental apparatus is constituted of two main parts. The first segment is the combustion part including the burner, the gas bottles and the flow controllers, while the second is the electric part composed of the DC power supply, the downstream electrode and the burner as a second electrode.

2.1. Geometrical and numerical model

The numerical geometry, based on the experimental system, is a 2D axisymmetric domain comprising the burner and the upstream electrode. Owing to the symmetrical geometry of the burner, only one half of the geometric domain was modeled to minimize the calculation cost (CPU). Since the flow is steady and the flame is stationary and laminar, the steady state was considered when resolving the governing equations. The governing equations are conservation of mass (1), momentum (2-3), energy (7) and species (9).

Continuity:

$$\frac{\partial(\rho u)}{\partial x}+\frac{1}{r}\frac{\partial(r\rho v)}{\partial r}=0 \qquad (1)$$

Where ρ is the density of gas, u is the x direction of flow velocity and v is the r direction of flow velocity.

x direction momentum:

$$\frac{\partial(\rho uu)}{\partial x}+\frac{1}{r}\frac{\partial(r\rho uv)}{\partial r}=-\frac{\partial p}{\partial x}+2\frac{\partial}{\partial x}\left(\mu\frac{\partial u}{\partial x}\right)+\frac{1}{r}\frac{\partial}{\partial r}\left(r\mu\frac{\partial u}{\partial r}\right)+\frac{1}{r}\frac{\partial}{\partial r}\left(r\mu\frac{\partial v}{\partial x}\right)-\rho g+F_x^e \qquad (2)$$

r direction momentum:

$$\frac{\partial(\rho uv)}{\partial x}+\frac{1}{r}\frac{\partial(r\rho vv)}{\partial r}=-\frac{\partial p}{\partial r}+\frac{\partial}{\partial x}\left(\mu\frac{\partial v}{\partial x}\right)+\frac{\partial}{\partial x}\left(\mu\frac{\partial u}{\partial r}\right)+\frac{2}{r}\frac{\partial}{\partial r}\left(r\mu\frac{\partial v}{\partial r}\right)-\frac{2\mu v}{r^2}+F_r^e \qquad (3)$$

Where μ is the dynamic viscosity, p is the pressure, g is the gravitational acceleration and F_x^e and F_r^e are the electric body force components.

The source terms in momentum equations can be given by Lorentz force as:

$$F_i^e=E_i e(n_+-n_-)=E_i e n_c \qquad (4)$$

Where E_i is the axial or the radial electric field intensity, e is the elementary charge, n_+ is the positive charge density, n_- is the negative charge density, and n_c is the net charge density.

The electric field strength is calculated by the mean of Poisson's equation:

$$\frac{\partial}{\partial \mathrm{x}}\left(\frac{\partial V}{\partial x}\right)+\frac{1}{r}\frac{\partial}{\partial r}\left(r\frac{\partial V}{\partial r}\right)=-\frac{e n_c}{\varepsilon_0} \qquad (5)$$

Here, V is the electric potential and ε_0 represents the permittivity of the free space.

The electric field is related to the electric potential by the simple differential equation:

$$\boldsymbol{E} = -\nabla V \tag{6}$$

Energy:

$$\frac{\partial(\rho u h)}{\partial x} + \frac{1}{r}\frac{\partial(r\rho v h)}{\partial r} = \frac{\partial}{\partial x}\left(k\frac{\partial T}{\partial x}\right) + \frac{1}{r}\frac{\partial}{\partial r}\left(rk\frac{\partial h}{\partial r}\right) - \sum_j \frac{\partial\left(h_j J_j^x\right)}{\partial x} - \sum_j \frac{1}{r}\frac{\partial\left(h_j J_j^r\right)}{\partial r} + \frac{\partial(\tau u)}{\partial x} + \frac{1}{r}\frac{\partial(\tau v)}{\partial r} + \dot{Q} + f \tag{7}$$

Where h corresponds to the total sensible enthalpy of the gas, k is the thermal conductivity, $\boldsymbol{J_j}$ and h_j are the diffusion flux and the sensible enthalpy of species j respectively, τ is the viscous dissipation stress, $\dot{Q}$ corresponds to the heat release due to combustion and f is the electric contribution in total energy transport equation.

Since the energy from the applied electric field f is weak compared to the burning thermal energy of ethylene, the electric field contribution in the total energy variation has been neglected.

Species:

$$\frac{\partial(\rho u Y_i)}{\partial x} + \frac{1}{r}\frac{\partial(r\rho v Y_i)}{\partial r} = -\frac{\partial\left(J_j^x\right)}{\partial x} - \frac{1}{r}\frac{\partial(r J_j^r)}{\partial r} + \omega_i \tag{8}$$

Where Y_i is the mass fraction of species i and ω_i is the net rate of production of species i by chemical reaction. The net rate of production, ω_i, is obtained by applying the laminar finite rate model using Arrhenius expression.

For neutral species, the diffusion flux of species is calculated using the dilute approximation (Fick's law) to model mass diffusion due to concentration gradients. For charged species, the electric diffusion flux was introduced to the molecular diffusion by the following relation:

$$\boldsymbol{J_i} = -\rho D_i \nabla Y_i + q_i \rho \kappa_i Y_i \boldsymbol{E} \tag{9}$$

Where D_i is the molecular diffusion coefficient, q_i is the specie charge (negative if the specie is negatively charged) and κ_i is the electric mobility.

For all the species except electrons, D_i was calculated by assuming a constant Schmidt number $Sc=0.7$. For the electrons, the diffusion coefficient D^e was computed by the mean of Einstein's relation as presented by equation (11):

$$D^e = \kappa^e k_b \frac{T}{e} \tag{10}$$

Where k_b is the Boltzmann constant $(1.38\times10\text{-}23\ J.K^{-1})$.

As supposed by Fialkov [26], a constant value of $1\ cm^2.s^{-1}.V^{-1}$ for the electric mobility was admitted for the ions. For the electrons, the relation of Delcroix [27] was employed to compute the electronic mobility:

$$\kappa^e = \left(\frac{m^0}{m^e}\right)^{0.5} \kappa_i \tag{11}$$

Where m^0 is the mass of gas and m^e is the electronic mass.

2.2. Chemical kinetic model and validation case

The numerical model was validated against the experimental case of Santoro et al. [28]. Santoro's experiment was performed using a co-flow burner with inner diameters of 10.5 mm and 97.7 mm for the central tube and the outer tube respectively. This burner was described in detail at the International Sooting Flame (ISF) Workshop [29]. The ethylene flow rate was fixed at 3.45 cm^3/sec corresponding to a mean velocity of 3.98 cm/sec with an air co-flow rate of 713.3 cm^3/sec. An 88 mm ethylene diffusion flame was developed and radial temperature and velocity measurements were taken at several HABs (Height Above the Burner) using thermocouple rapid insertion and laser velocimetry techniques. The computational domain for Santoro's case is about 14×6 cm as shown by the Figure 1 and a non-uniform quadrilateral grid was created with a resolution of 180×100 control volumes.

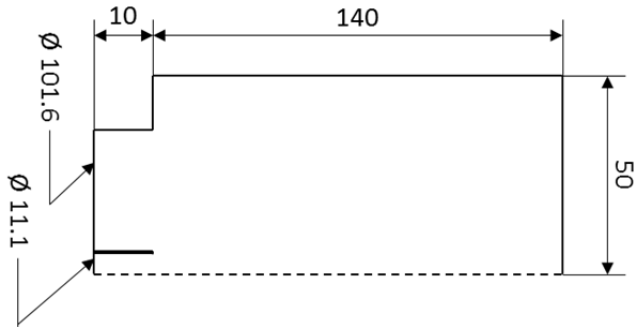

Figure 1. Computational geometry of Santoro burner experiment (distance in mm)

To simulate ethylene combustion, four reaction schemes were tested: a two-steps reaction scheme, a ten-step reaction scheme and a skeletal scheme Z66 with (designed by 2) and without (designed by 1) soot radiation loss. The tested schemes are presented in Table 1.

Table 1. Tested reaction schemes

Reaction scheme	# of species	Radiation model	# of reactions	Ref
Two steps	6	1	2	[30]
Ten steps	9	1	10	[31]
Skeletal Z66(1)	23	1	66	[32]
Skeletal Z66(2)	23	2	66	[32]

The transport and thermodynamics data are taken from GRI-mech 3.0 [33].

For an important part of the produced energy is lost by radiation, the thermal radiation loss was computed under the assumption of optically thin heat transfer between the flame and the cold surroundings. The thermal energy loss due to radiation under this approach is given by the following expression:

$$\dot{Q}_{loss} = 4\sigma\left(T^4 - T_b^4\right)\left(\sum_i \left(p_i a_{pi}\right) + k_{s,Plank}\right) \quad (12)$$

Where σ is the Stefan-Boltzmann constant ($5.669\text{x}10^{-8}$ W.m^{-2}.K^{-4}), T is the local temperature, T_b is the atmospheric temperature (fixed at 298 K), p_i is the local partial pressure of species i, a_{pi} is the Plank mean absorption coefficient. In the first three cases, only the radiation energy lost by H_2O, CO_2 and CO (if it exists in the scheme) was considered, whereas in the fourth case, the radiation loss by soot is added to the gaseous species radiation loss. In this case, soot characteristics were calculated by resolving a simplified Moss-Brookes model. Plank mean absorption coefficient for gaseous species

was fitted using n-th degree Gaussian functions based on [34]; $k_{s,Plank}$ was calculated by applying the following expression [35]:

$$k_{s,Plank} = 1464 \times f_s T \qquad (13)$$

Where f_s is the soot volume fraction and T is the local temperature.

The choice of the chemical schemes and the validation of the numerical model were performed according to the measured axial velocity and temperature profiles of Santoro's experimental data [28]. In the Figure 2, the computed results are presented for several reaction schemes against Santoro et al. measurements [28]. Obviously, the more the chemical reaction model is detailed, the more it is accurate. As expected, the skeletal mechanism gives the most precise results and well predicts the temperature and the axial velocity throughout the flame.

At the region near the burner tip (HAB= 3 and 5 mm), the calculated values of the axial velocity peaks are overestimated. In this region, velocity and temperature are particularly sensitive to the injection conditions since several aerodynamic phenomena (burner preheating and friction loss at the burner wall) could interact and influence the experimental measurements. Indeed, the effect of burner preheating is observed in the difference of temperature values between the experiment and the model at the flame axis. This effect was also observed by other numerical studies [36,37]. A good agreement with the experiment is obtained especially in temperature profiles at HAB 20, 50 and 70 mm. The difference between the experimental and numerical curves could be attributed to the soot model which plays a key role in estimating the radiation loss and therefore the temperature calculation. This aspect is highlighted by the significant difference between curves with and without considering soot.

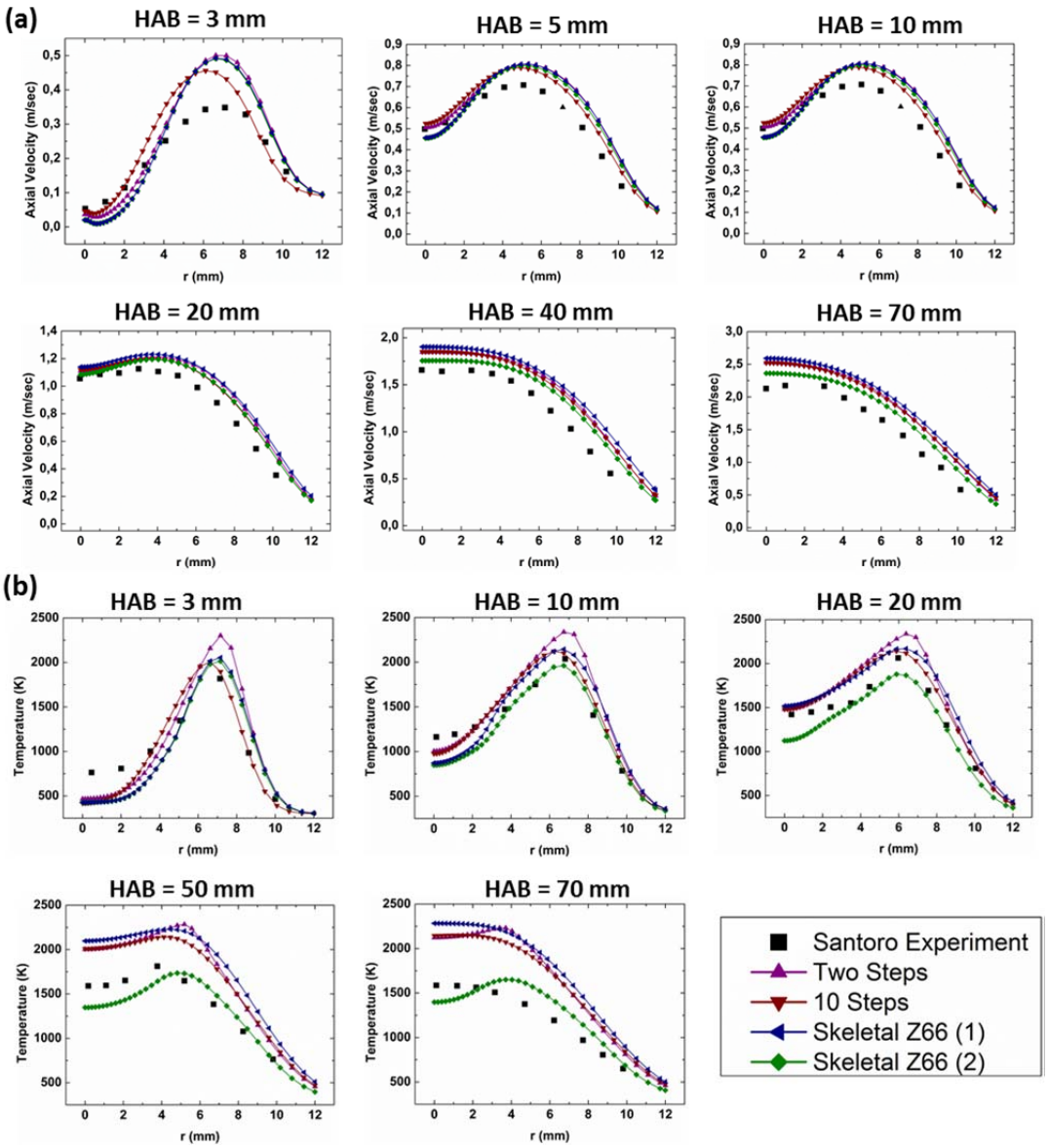

Figure 2. Computed axial velocity (a) and temperature (b) of the validation cases compared to Santoro's measurements [28]

In order to check the role of burner preheating and the ability of the model to reproduce the experimental results, the temperature of the fuel at the burner exit was increased to 600 K as proposed by Boedeker et al. [36]. Then, the computed temperature with fuel preheating are compared to the measured values of Snelling et al. [38] and Sun et al. [39]. Figure 3 presents the computed temperature distribution compared to the temperature field measured by Sun et al. [39] using non-linear Two-Line Atomic Fluorescence (nTLAF). Figure 4 shows the computed values of radial temperature distribution at HAB of 10, 20, 40 and 50 mm (Figure 4(a)-(d)) and the temperature profile along the flame axis compared to Snelling et al. measurements [38] performed by the mean of Coherent anti-Stokes Raman

Spectroscopy technique (CARS) and Sun et al. [39] values (Figure 4(e)). The computed temperature field is in close agreement with the measured one in terms of values and distribution as revealed by the Figure 4. Accordingly, the developed numerical model coupled with the skeletal mechanism can be used to simulate ethylene combustion in a co-flow configuration (with computing soot radiation loss.

As a result, the skeletal kinetic reaction mechanism (2) was selected to model ethylene-air combustion in this study. In this mechanism, the two radicals CH and O which are the parents of the first ion are included.

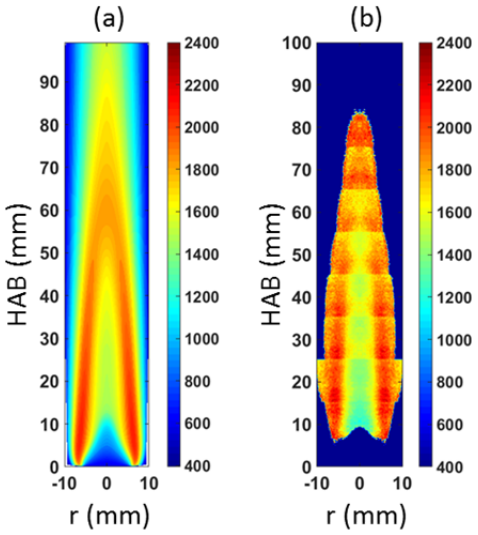

Figure 3. Comparison between (a) computed temperature and (b) temperature field measured by nTLAF technique [39]

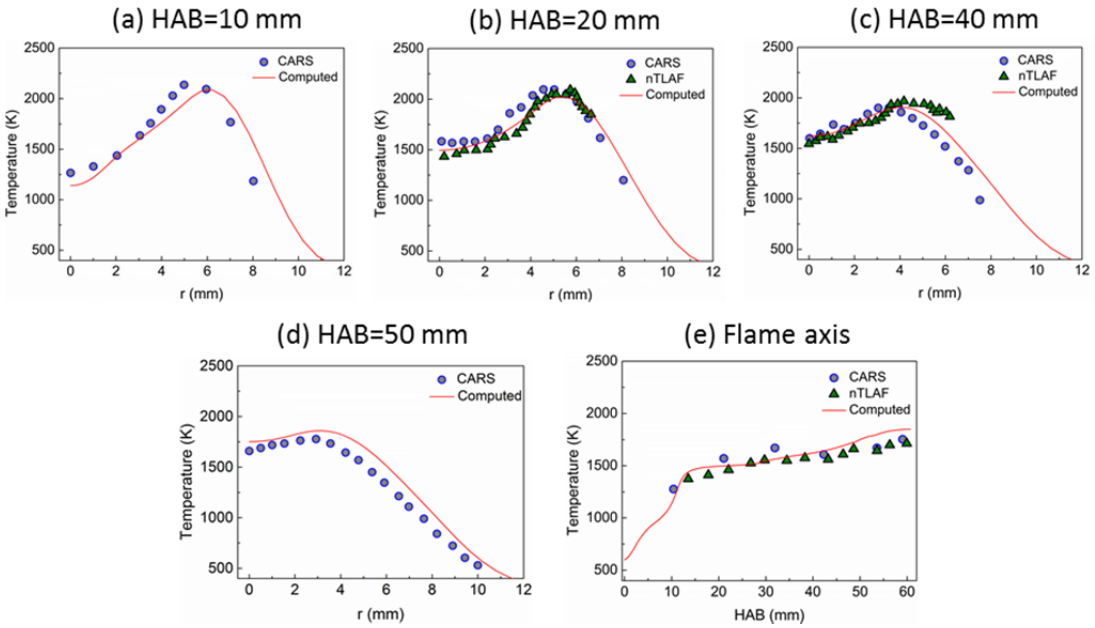

Figure 4. (a-d) Radial distribution of the computed and measured temperature (by CARS [38] and nTLAF [39] techniques) at HAB of 10, 20, 40 and 50 mm. (e) Axial evolution of the computed and measured temperature along the flame axis.

2.3. Kinetics of charged species and boundary conditions

Since the concentration of charged species is always lower than the concentration of any neutral species present in the mechanism, six reactions were added including the three charged species: HCO^+, H_3O^+ (the most abundant cation) and electron. These reactions include two reactions for H_3O^+ formation and four reactions for charge recombination as described in the Table 2.

Table 2. Integrated ions schemes in the model

Reaction	A	n	E	Reference
$CH+OH \Leftrightarrow CO^++e^-$	$2.51x10^{11}$	0	7.12	[40]
$HCO^++H_2O \Leftrightarrow H_3O^++CO$	$1.51x10^{15}$	0	0	[41]
$H_3O^++e^- \Leftrightarrow H_2O+H$	$2.29x10^{18}$	-0.5	0	[42]
$H_3O^++e^- \Leftrightarrow OH+H+H$	$7.95x10^{21}$	-1.4	0	[42]
$H_3O^++e^- \Leftrightarrow H_2+OH$	$1.25x10^{19}$	-0.5	0	[42]
$H_3O^++e^- \Leftrightarrow O+H_2+H$	$6x10^{17}$	-0.3	0	[42]
Units are cm, mol, s, kJ and K				

In this study, only the positive ions are taken into consideration. If negative ions have been shown to play an important role in the effect of electric field on flames, they were not taken into account here for two reasons: their concentration is systematically lower than the positive ones and they are rapidly dissipated due to the proximity of the flame to the positive electrode.

Boundary conditions were adapted to the experimental conditions [25] as presented in the Figure 5. The injection conditions were those used in the experiment (ethylene flow rate of 3.1 cm^3/sec and air co-flow rate of 72 cm^3/sec). These conditions are detailed in the Table 3. In the experiment, the upstream electrode, a horizontal grid placed at 140 mm above the burner, is set at 0 potential value (grounded electrode). Here, in the numerical model, this condition was satisfied by fixing the outlet potential value to 0 kV.

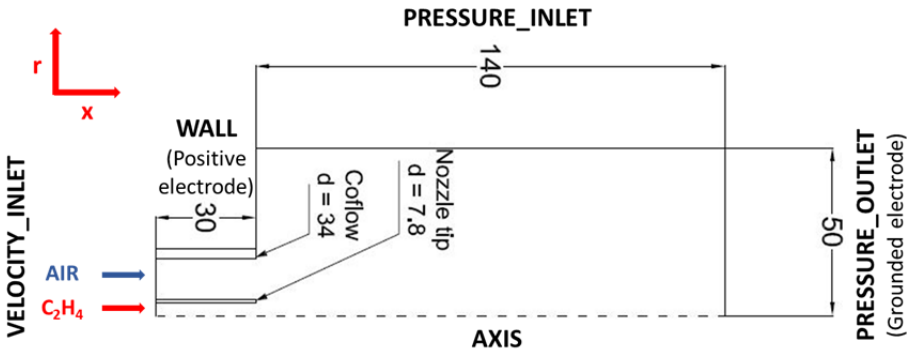

Figure 5. Computational geometry reproducing the experimental setup of [25] (distance in mm)

A non-uniform quadrilateral mesh of 30000 nodes (250×120 of resolution) was generated. It was refined at the symmetry axis and near the nozzle tip (flame region). A grid convergence study was performed by simulating the reacting flow with one-step reaction scheme. A medium grid was chosen as the best compromise between results accuracy and calculation cost.

The governing equations were solved using a pressure based implicit solver. For the spatial derivative, the 'Least Squares Cell-Based Gradient Evaluation' method was adopted. The ethylene was ignited above the burner exit by assuming a temperature of 2000 K. Calculations were performed until convergence.

Table 3. Boundary conditions

	Boundary	**Conditions**
Fuel exit	VELOCITY_INLET	Y_{C2H4} = 1; T = 298 K; Potential flux = 0; Axial velocity = 6,5 cm/sec; Radial velocity = 0 cm/sec
Air exit	VELOCITY_INLET	Y_{O2} = 0,23; T = 298 K; flux de potential = 0; Axial velocity = 6 cm/sec; Radial velocity = 0 cm/sec
Burner	WALL	T = 298 K Potential = {0; 5; 10; 15; 20}
Atmospheric air	PRESSURE_INLET	Y_{O2} = 0,23; T = 298 K; Potential flux= 0
Symmetry axis	AXIS	_
Outlet	PRESSURE_OUTLET	Y_{O2} = 0,23; T = 298 K; Potential = 0 kV

2. Results and discussion

3.1 Flame shape and luminosity

Figure 6 shows the comparison between a visible flame image captured during an experiment and the calculated flame temperature contour where no electric field is applied. It reveals that the computed flame shape is intimately similar to the flame contour given by the image.

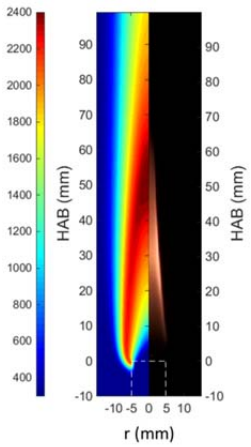

Figure 6. Simulated temperature field and visible flame image without an electric field

Figure 7. Radial distribution of luminosity and computed temperature at HABs 15.5, 19.5, 29 and 39 mm. displays the radial distribution of deconvoluted luminosity (by Abel's inversion) taken from flame imaging during an experiment and computed temperature at several HABs without an electric field. The high sooting zones in the radial section of the flame correspond to the high luminosity regions where a high concentration of particles is responsible for a large part of the luminous emission of the flame. The luminosity decreases with the decrease of the volume fraction of soot that stops forming by approaching higher temperature zones. A similar trend has been observed by comparing the transmittance curves measured by Santoro et al. [43] and the measured temperature at the equivalent HABs [28].

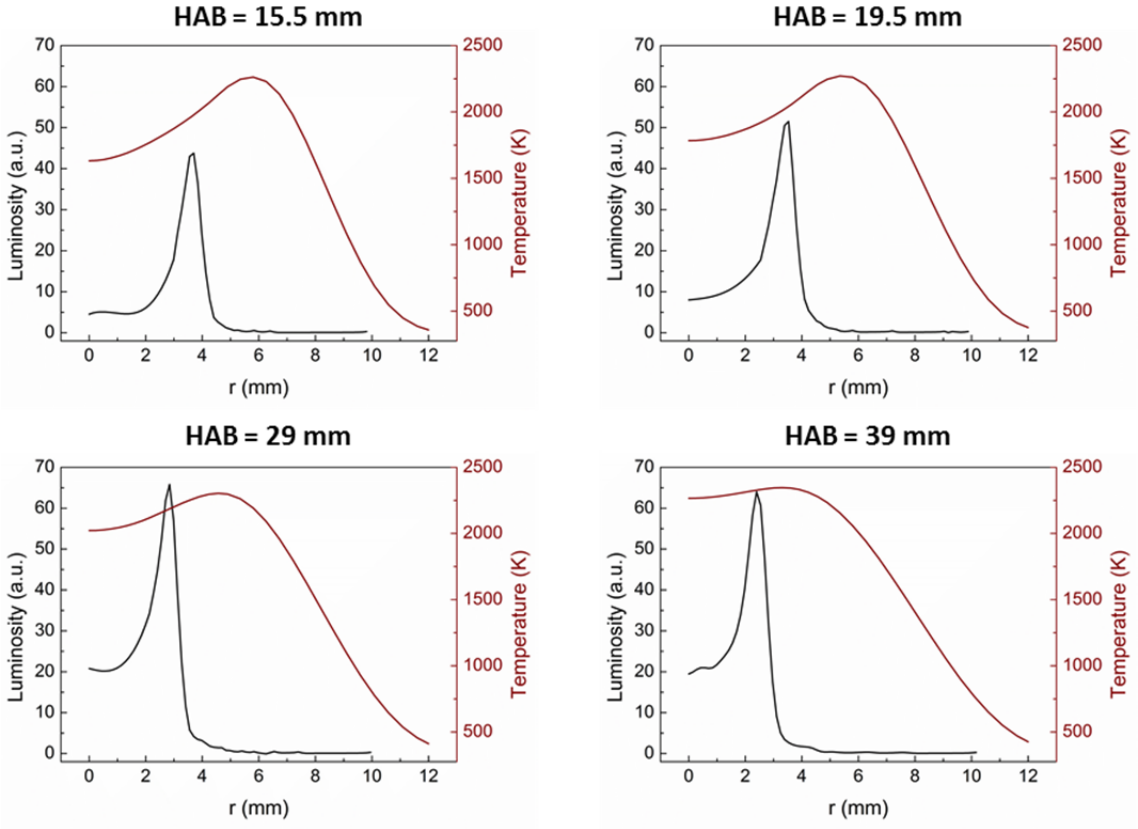

Figure 7. Radial distribution of luminosity and computed temperature at HABs 15.5, 19.5, 29 and 39 mm.

3.2. Electric effects on ethylene flame

Figure 8. Simulated OH mole fraction field under different values of applied potential presents the computed OH mole fraction contour of the flame at different voltages applied to the burner: 0, 5, 10, 15 and 20 kV. The solid black line corresponds to a value of 5×10^{-3} OH mole fraction; this value corresponds to the stoichiometric front and is attained by calculating the equilibrium state of ethylene-air mixture near

the stoichiometry using the detailed scheme (Aramco 2.0 [44]). This line was added to monitor the flame shape change with the electric field intensity.

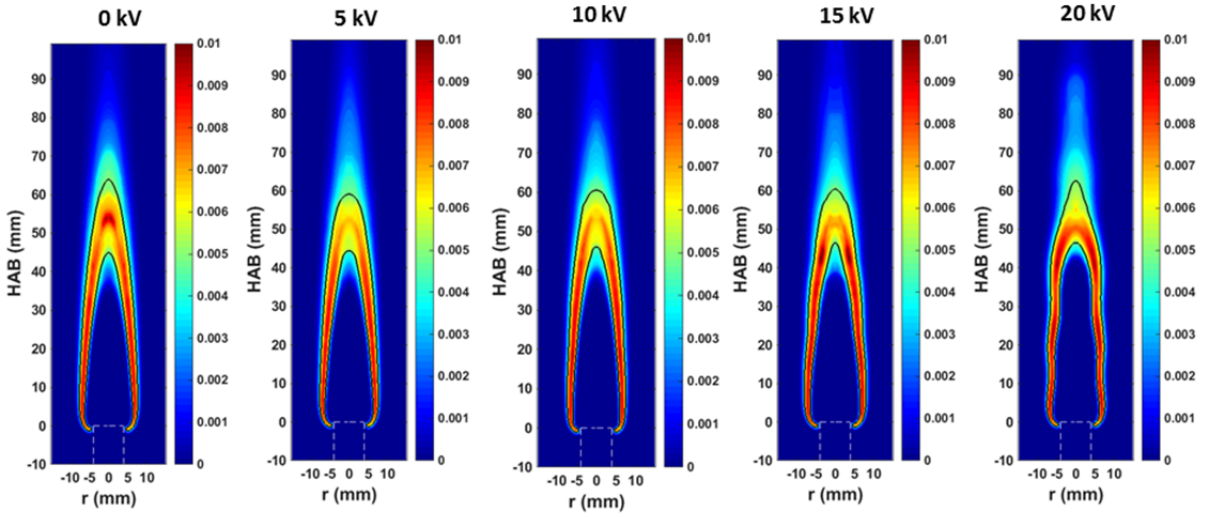

Figure 8. Simulated OH mole fraction field under different values of applied potential

Interestingly, modifications in the flame form are remarked when we apply an electric field. The line tip appears flat at both 5 and 10 kV instead of its pointed form in normal case as shown in Figure 8. The same observation was remarked during the experiments at 5 and 10 kV as shown in Figure 9. In this figure, the white line represents a value of 30 pixel light intensity. The areas of the flame tip at 0, 5 and 10 kV are presented in Figure 10. These areas correspond to the surfaces formed by the iso-line (OH contour in numerical case or pixel intensity contour in the experimental case) between the flame tip and 3 mm below this point. These areas are then divided by the flame tip area at 0 kV. Figure 10 represents the same trend of the numerical results compared to the experiment: the flame tip area becomes larger as the applied potential at the burner is increased.

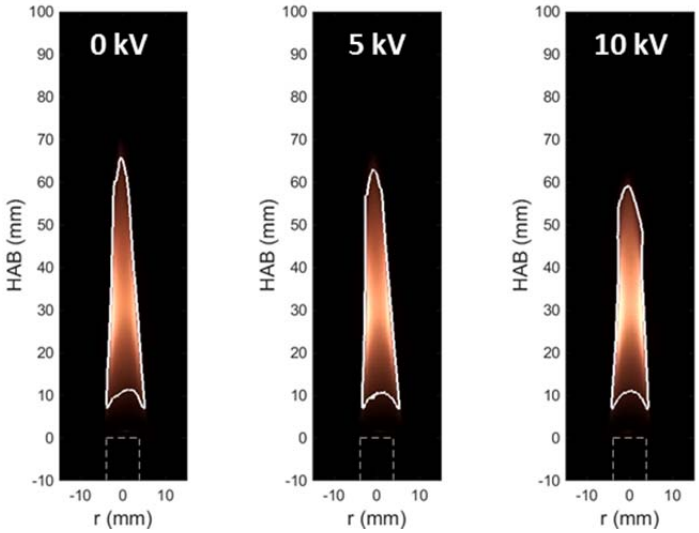

Figure 9. Flame images taken during an experiment at 3 different values of applied potential

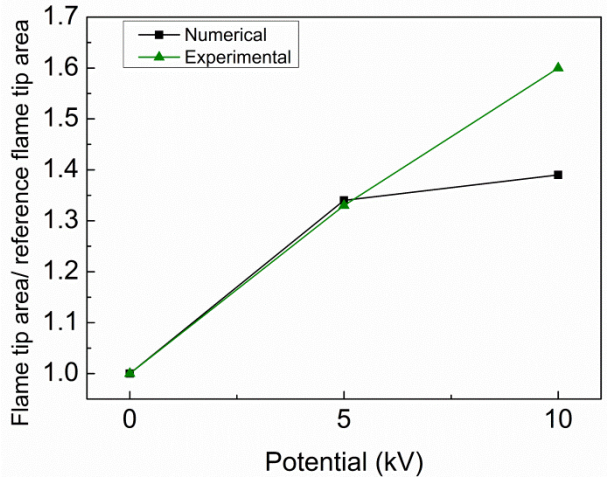

Figure 10. Flame tip area as function of applied potential for experimental and numerical case.

Furthermore, a slight decrease in flame length is observed for 5 and 10 kV voltages. This decrease was also noted experimentally but with a more significant contrast [25,45]. The flame shape at voltage 15 kV shows a local perturbation near the flame tip, while it is globally deformed at 20 kV. The flame at 15 kV marks a transitional state to a new regime as shown in the last two plots in Figure 8. This behavior corresponds to what has been experimentally detected when instabilities start to appear under high voltages. Hence, the numerical model qualitatively reproduces the experimental observations under the effect of an electric body force.

Two main mechanisms have been proposed [25,45] to explain the decrease in flame length: an enhancement in mixing and an elevation in burning rate. In order to investigate this effect, the maximum C_2H_4 consumption rate is presented as function of the applied voltage in Figure 11. As

expected, the fuel consumption rate, presented here by the reaction rate, increases with the electric potential. The higher the consumption rate is, the greater the amount of fuel per unit volume and time is burned. This fact could indicate a better mixing between fuel and air which is generated by the electric field action on the interaction between the charged species and the flow. This mixing enhances the combustion process and could entrain an increase in the maximal OH mole fraction as shown in Figure 8. The influence of the electric field on the flame propagation velocity was also reported by several experimental studies [46,47].

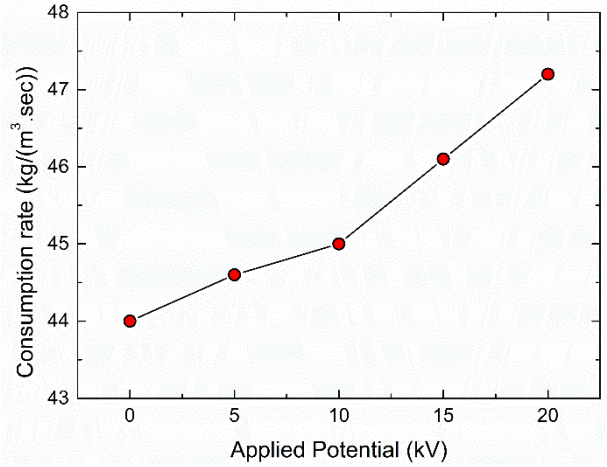

Figure 11. Maximum computed consumption rate of C_2H_4 as function of applied potential

In order to better understand the effect of electric field on the flow and flame behaviors, Figure 12 presents the computed velocity (a) and temperature distribution (b) at different HABs (presented by line colors) under 5 voltage values (presented by line styles). Noticeably, the electric field affects the velocity in the low region of the flame, whereas a minor effect is detected upstream (HAB= 50 mm). The electric field tends to slow down the flow in front of the flame front though the velocity is increased on both sides. Figure 12-a shows that the electrically-induced reduction of velocity is located specifically at the reaction zone. Hence, it is related to the production rate of ions by chemi-ionization. Besides, when the electric voltage rises, the maximum velocity decreases. The drift velocity due to the positive ions motion is directed downwards in a positive voltage. It is proportional to the net charge density and field intensity as described by equation (4). The ionic wind that results from the positive charge displacement and their collisions with neutral leads to the reduction of fluid flow from the injection. The increased velocity at the periphery of the flame is causing an increase of

the air entrainment along the flame, entrainment already described also by Yamashita et al. [15]. Accordingly, better blending leads to an enhanced combustion rate.

In the temperature profiles of Figure 12-b, no obvious changes were detected in the reaction zone. However, an increase of temperature, systematically observed on the outer side of the flame, affirms the extension of the reaction zone. Therefore, this confirms the existence of an enhanced mixing by the entrained air.

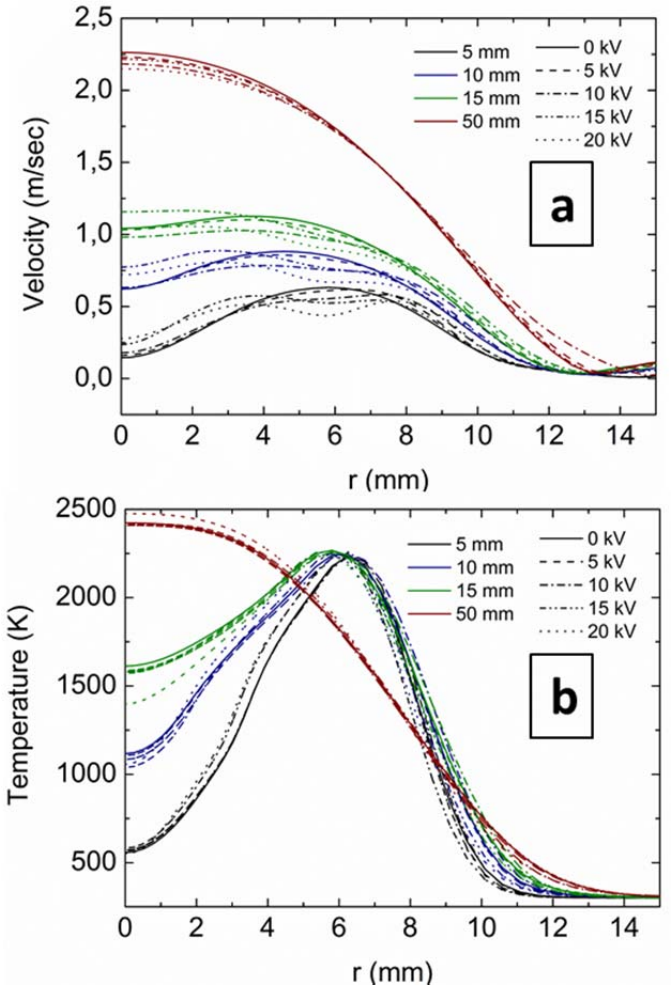

Figure 12. (a) Computed velocity and (b) temperature distribution at different HABs and 5 potential values

Figure 13 represents the distribution of H_3O^+ molar concentration at 0 and 10 kV and the difference of H_3O^+ molar concentration between 0 and 10 kV. As evidenced by the figure, most of H_3O^+molecules are concentrated near the burner zone. Hence, the electric field could act directly on the flow field in this low region of the flame as shown in Figure 12(a). An increase of H_3O^+concentration is also detected when an electric field is applied. This elevation is concentrated in the low flame region where

an air entrainment favors the mixing, enhances the combustion rate and promotes the ion production. Such enhancement leads to a greater action of the electric force on the flow and could generate flame deformations as observed in the Figure 8 at higher potential values.

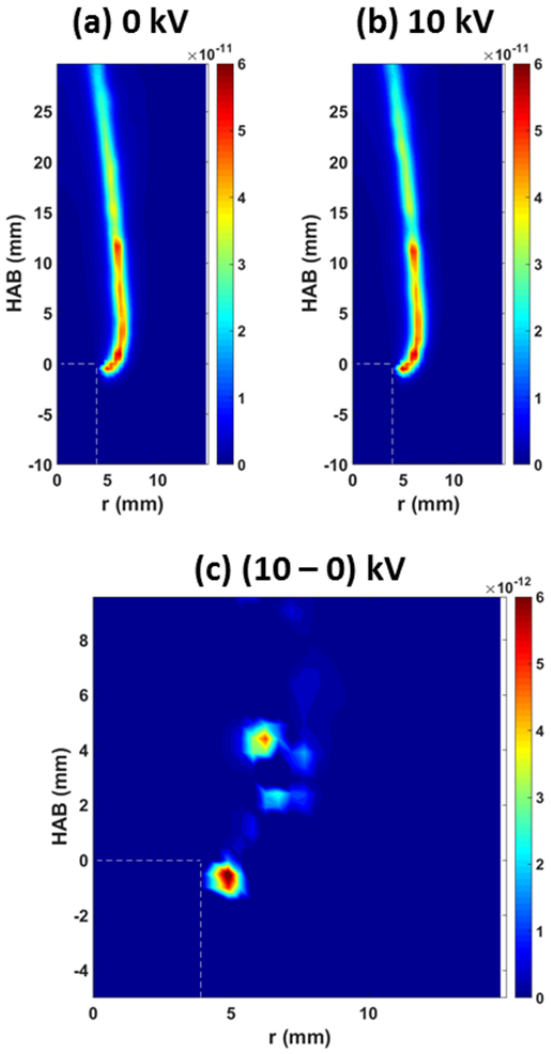

Figure 13. H_3O^+ molar concentration distribution at (a) 0kV and (b) 10 kV. (c) difference of H_3O^+ molar concentration between 10 kV and 0 kV cases (unit in kmol/cm^3).

3.3. Linking experimental and numerical results

In the experiment, a noticeable reduction of soot volume fraction was detected with an important change in flame structure (flame shortness and enlargement). Yet, in the numerical approach, several modifications are detected which are consistent with the experiment. Soot formation and oxidation is highly dependent on velocity, temperature and species distribution. By providing the modified flow field and thermal profiles including the action of the ionic wind; the numerical model could explain several experimental observations: the diminution in flame height may be referred to an elevation in

burning rate due to the electric body forces effect especially in a zone near the burner, and the increase in OH mole fraction promotes the oxidation of particles and participates in the reduction of soot [48]. The electric field effects are extremely intensive in the low flame region where the charged species are concentrated (Figure 13). As most of particles and soot precursors are positively charged as reported by Chen et al. [49], the proximity of the fuel electrode where they are attracted by the Lorentz force reduces their residence time and the potential for their formation. Nevertheless, the kinetic of these particles should be developed with the transport properties to be able to simulate the interaction between an electric field and particles. Such work remains an open topic of combustion researchers to model the electric aspect of soot formation and the effect of electric field on this process.

Conclusion

A simplified model has been developed to elucidate the effect of electric body forces on an ethylene non-premixed combustion. The kinetic model was first validated against collected experimental data from literature. The comprehensive model including the electric field calculation and the charged particles distribution was able to reproduce the experimental observations. The electric field was proved to affect the flow field at the burner exit by acting on both the flame structure and the burning process. Future works should embrace a more detailed model comprising an electrical diffusion model of charged species, more detailed charged particles chemistry and a soot model with charged particles to have a better understanding of the influence of electric field on diffusion combustion and soot formation.

Acknowledgments

The research reported in this publication was supported by labex Caprysses, (Convention ANR-11-LABX 0006-01), CNRS and Orleans University.
The authors acknowledge the participation of B. Sarh in the rereading of the manuscript.

References

[1] Ju Y, Sun W. Plasma assisted combustion: Dynamics and chemistry. Prog Energy Combust Sci 2015;48:21–83. https://doi.org/10.1016/j.pecs.2014.12.002.

[2] Chen Z, Li Z, Zhu Q, Jing J. Gas/particle flow and combustion characteristics and NOx emissions of a new swirl coal burner. Energy 2011;36:709–23. https://doi.org/10.1016/j.energy.2010.12.037.

[3] Liu Y, Sun X, Sethi V, Nalianda D, Li Y-G, Wang L. Review of modern low emissions combustion technologies for aero gas turbine engines. Prog Aerosp Sci 2017;94:12–45. https://doi.org/10.1016/j.paerosci.2017.08.001.
[4] Kim GT, Park DG, Cha MS, Park J, Chung SH. Flow instability in laminar jet flames driven by alternating current electric fields. Proc Combust Inst 2017;36:4175–82. https://doi.org/10.1016/j.proci.2016.09.015.
[5] Kim MK, Ryu SK, Won SH, Chung SH. Electric fields effect on liftoff and blowoff of nonpremixed laminar jet flames in a coflow. Combust Flame 2010;157:17–24. https://doi.org/10.1016/j.combustflame.2009.10.002.
[6] Won SH, Cha MS, Park CS, Chung SH. Effect of electric fields on reattachment and propagation speed of tribrachial flames in laminar coflow jets. Proc Combust Inst 2007;31:963–70. https://doi.org/10.1016/j.proci.2006.07.166.
[7] Saito M, Arai T, Arai M. Control of soot emitted from acetylene diffusion flames by applying an electric field. Combust Flame 1999;119:356–66. https://doi.org/10.1016/S0010-2180(99)00065-6.
[8] Xiong Y, Cha MS, Chung SH. AC electric field induced vortex in laminar coflow diffusion flames. Proc Combust Inst 2015;35:3513–20. https://doi.org/10.1016/j.proci.2014.08.027.
[9] Park DG, Choi BC, Cha MS, Chung SH. Soot Reduction Under DC Electric Fields in Counterflow Non-Premixed Laminar Ethylene Flames. Combust Sci Technol 2014;186:644–56. https://doi.org/10.1080/00102202.2014.883794.
[10] Chien Y-C, Escofet-Martin D, Dunn-Rankin D. Ion current and carbon monoxide release from an impinging methane/air coflow flame in an electric field. Combust Flame 2019;204:250–9. https://doi.org/10.1016/j.combustflame.2019.03.022.
[11] Vega EV, Shin SS, Lee KY. NO emission of oxygen-enriched CH4/O2/N2 premixed flames under electric field. Fuel 2007;86:512–9. https://doi.org/10.1016/j.fuel.2006.07.034.
[12] Kuhl J, Seeger T, Zigan L, Will S, Leipertz A. On the effect of ionic wind on structure and temperature of laminar premixed flames influenced by electric fields. Combust Flame 2017;176:391–9. https://doi.org/10.1016/j.combustflame.2016.10.026.
[13] Lacoste DA, Xiong Y, Moeck JP, Chung SH, Roberts WL, Cha MS. Transfer functions of laminar premixed flames subjected to forcing by acoustic waves, AC electric fields, and non-thermal plasma discharges. Proc Combust Inst 2017;36:4183–92. https://doi.org/10.1016/j.proci.2016.05.034.
[14] Tinajero J, Dunn-Rankin D. Non-premixed axisymmetric flames driven by ion currents. Combust Flame 2019;199:365–76. https://doi.org/10.1016/j.combustflame.2018.10.036.
[15] Yamashita K, Karnani S, Dunn-Rankin D. Numerical prediction of ion current from a small methane jet flame. Combust Flame 2009;156:1227–33.
[16] Belhi M, Domingo P, Vervisch P. Modelling of the effect of DC and AC electric fields on the stability of a lifted diffusion methane/air flame. Combust Theory Model 2013;17:749–87. https://doi.org/10.1080/13647830.2013.802415.
[17] Belhi M, Domingo P, Vervisch P. Direct numerical simulation of the effect of an electric field on flame stability. Combust Flame 2010;157:2286–97. https://doi.org/10.1016/j.combustflame.2010.07.007.
[18] Rao R, Honnery D. A simplified mechanism for the prediction of the ion current during methane oxidation in engine-like conditions. Combust Flame 2015;162:2928–36. https://doi.org/10.1016/j.combustflame.2015.03.011.
[19] Xu T, Chen Q, Zhang B, Lu S, Mo D, Zhang Z, et al. Effects of electric field on micro-scale flame properties of biobutanol fuel. Sci Rep 2016;6. https://doi.org/10.1038/srep32938.
[20] Luo Y, Gan Y, Xu J, Yan Y, Shi Y. Effects of electric field intensity and frequency of AC electric field on the small-scale ethanol diffusion flame behaviors. Appl Therm Eng 2017;115:1330–6. https://doi.org/10.1016/j.applthermaleng.2016.11.145.
[21] Luo Y, Gan Y, Jiang X. Investigation of the effect of DC electric field on a small ethanol diffusion flame. Fuel 2017;188:621–7. https://doi.org/10.1016/j.fuel.2016.10.073.

[22] Belhi M, Lee BJ, Bisetti F, Im HG. A computational study of the effects of DC electric fields on non-premixed counterflow methane-air flames. J Phys Appl Phys 2017;50:494005. https://doi.org/10.1088/1361-6463/aa94bb.
[23] Belhi M, Han J, Casey TA, Chen J-Y, Im HG, Sarathy SM, et al. Analysis of the current–voltage curves and saturation currents in burner-stabilised premixed flames with detailed ion chemistry and transport models. Combust Theory Model 2018;22:939–72. https://doi.org/10.1080/13647830.2018.1468033.
[24] Belhi M, Lee BJ, Cha MS, Im HG. Three-dimensional simulation of ionic wind in a laminar premixed Bunsen flame subjected to a transverse DC electric field. Combust Flame 2019;202:90–106. https://doi.org/10.1016/j.combustflame.2019.01.005.
[25] Sayed-Kassem A, Gillon P, Idir M, Gilard V. On the Effect of a DC Electric Field on Soot Particles' Emission of a Laminar Diffusion Flame. Combust Sci Technol 2019:1–12. https://doi.org/10.1080/00102202.2019.1678901.
[26] Fialkov AB. Investigations on ions in flames. Prog Energy Combust Sci 1997;23:399–528. https://doi.org/chen.
[27] Delcroix JL. Physique des plasmas. Dunod; 1966.
[28] Santoro RJ, Yeh TT, Horvath JJ, Semerjian HG. The Transport and Growth of Soot Particles in Laminar Diffusion Flames. Combust Sci Technol 1987;53:89–115. https://doi.org/10.1080/00102208708947022.
[29] Laminar Flames | International Sooting Flame (ISF) Workshop | University of Adelaide n.d. http://www.adelaide.edu.au/cet/isfworkshop/data-sets/laminar-flames (accessed July 1, 2020).
[30] Westbrook CK, Dryer FL. Simplified Reaction Mechanisms for the Oxidation of Hydrocarbon Fuels in Flames. Combust Sci Technol 1981;27:31–43. https://doi.org/10.1080/00102208108946970.
[31] Singh DJ, Jachimowski CJ. Quasiglobal reaction model for ethylene combustion. AIAA J 1994;32:213–6. https://doi.org/10.2514/3.11972.
[32] Zettervall N, Fureby C, Nilsson EJK. Small Skeletal Kinetic Reaction Mechanism for Ethylene–Air Combustion. Energy Fuels 2017;31:14138–49. https://doi.org/10.1021/acs.energyfuels.7b02078.
[33] Gregory P. Smith, David M. Golden, Michael Frenklach, Nigel W. Moriarty, Boris Eiteneer, Mikhail Goldenberg, C. Thomas Bowman, Ronald K. Hanson, Soonho Song, William C. Gardiner, Jr., Vitali V. Lissianski, and Zhiwei Qin. GRI-Mech 3.0 n.d. http://www.me.berkeley.edu/gri_mech/ (accessed September 24, 2019).
[34] Maciej Chmielewski, Gieras M. Planck Mean Absorption Coefficients of H2O, CO2, CO and NO for radiation numericalmodeling in combusting flows. J Power Technol 2015;95:97–104.
[35] Demarco R. Modelling thermal radiation and soot formation in buoyant diffision flames. thesis. Aix-Marseille, 2012.
[36] Boedeker LR, Dobbs GM. Soot distribution and cars temperature measuremnts in axisymmetric laminar diffusion flames with several fuels. Symp Int Combust 1988;21:1097–105. https://doi.org/10.1016/S0082-0784(88)80340-0.
[37] Smooke MD, McEnally CS, Pfefferle LD, Hall RJ, Colket MB. Computational and experimental study of soot formation in a coflow, laminar diffusion flame. Combust Flame 1999;117:117–39. https://doi.org/10.1016/S0010-2180(98)00096-0.
[38] Hadef R, Geigle KP, Zerbs J, Sawchuk RA, Snelling DR. The concept of 2D gated imaging for particle sizing in a laminar diffusion flame. Appl Phys B 2013;112:395–408. https://doi.org/10.1007/s00340-013-5507-1.
[39] Sun Z, Dally B, Alwahabi Z, Nathan G. The effect of oxygen concentration in the co-flow of laminar ethylene diffusion flames. Combust Flame 2020;211:96–111. https://doi.org/10.1016/j.combustflame.2019.09.023.
[40] Gardiner WC, editor. Combustion Chemistry. New York, NY: Springer New York; 1984. https://doi.org/10.1007/978-1-4684-0186-8.

[41] Pedersen T, Brown RC. Simulation of electric field effects in premixed methane flames. Combust Flame 1993;94:433–48. https://doi.org/10.1016/0010-2180(93)90125-M.
[42] Prager J, Riedel U, Warnatz J. Modeling ion chemistry and charged species diffusion in lean methane–oxygen flames. Proc Combust Inst 2007;31:1129–37. https://doi.org/10.1016/j.proci.2006.07.141.
[43] Santoro RJ, Semerjian HG, Dobbins RA. Soot particle measurements in diffusion flames. Combust Flame 1983:203–18.
[44] AramcoMech 2.0 - NUI Galway n.d. http://c3.nuigalway.ie/combustionchemistrycentre/mechanismdownloads/aramcomech20/ (accessed February 10, 2020).
[45] Gillon P, Gilard V, Idir M, Sarh B. Electric field influence on the stability and the soot particles emission of a laminar diffusion flame. Combust Sci Technol 2019;191:325–38. https://doi.org/10.1080/00102202.2018.1467404.
[46] Li Y, Wang J, Xia H, Li C, Zhang M, Wu X, et al. Effect of DC electric field on laminar premixed spherical propagation flame at elevated pressures up to 0.5 MPa. Combust Sci Technol 2018;190:1900–22. https://doi.org/10.1080/00102202.2018.1467407.
[47] Li C, Wu X, Li Y, Wei X. Experimental study of positive and negative DC electric fields in lean premixed spherically expanding flames. Fuel 2017;193:22–30. https://doi.org/10.1016/j.fuel.2016.12.001.
[48] Shaddix CR, Smyth KC. Laser-induced incandescence measurements of soot production in steady and flickering methane, propane, and ethylene diffusion flames. Combust Flame 1996;107:418–52. https://doi.org/10.1016/S0010-2180(96)00107-1.
[49] Chen B, Wang H, Wang Z, Han J, Alquaity ABS, Wang H, et al. Ion chemistry in premixed rich methane flames. Combust Flame 2019;202:208–18. https://doi.org/10.1016/j.combustflame.2019.01.009.